THE JOURNAL OF BIOLOGICAL CHEMISTRY VOL. 291, NO. 49, pp. 25617–25628, December 2, 2016

Electrostatic and Structural Bases of Fe^{2+} Translocation through Ferritin Channels*[S]

Received for publication, July 12, 2016, and in revised form, October 3, 2016 Published, JBC Papers in Press, October 18, 2016, DOI 10.1074/jbc.M116.748046

Balasubramanian Chandramouli[‡§1], Caterina Bernacchioni[¶], Danilo Di Maio[‡§], Paola Turano[¶], and Giuseppe Brancato[‡§2]

From the [‡]Scuola Normale Superiore, Piazza dei Cavalieri 7, I-56126 Pisa, the [§]Istituto Nazionale di Fisica Nucleare (INFN) Sezione di Pisa, Largo Bruno Pontecorvo 3, 56127 Pisa, and the [¶]Magnetic Resonance Center (CERM) and Department of Chemistry, University of Florence, Via L. Sacconi 6, 50019 Sesto Fiorentino, Italy

Edited by F. Peter Guengerich

Ferritin molecular cages are marvelous 24-mer supramolecular architectures that enable massive iron storage (>2000 iron atoms) within their inner cavity. This cavity is connected to the outer environment by two channels at C3 and C4 symmetry axes of the assembly. Ferritins can also be exploited as carriers for *in vivo* imaging and therapeutic applications, owing to their capability to effectively protect synthetic non-endogenous agents within the cage cavity and deliver them to targeted tissue cells without stimulating adverse immune responses. Recently, X-ray crystal structures of Fe^{2+}-loaded ferritins provided important information on the pathways followed by iron ions toward the ferritin cavity and the catalytic centers within the protein. However, the specific mechanisms enabling Fe^{2+} uptake through wild-type and mutant ferritin channels is largely unknown. To shed light on this question, we report extensive molecular dynamics simulations, site-directed mutagenesis, and kinetic measurements that characterize the transport properties and translocation mechanism of Fe^{2+} through the two ferritin channels, using the wild-type bullfrog *Rana catesbeiana* H′ protein and some of its variants as case studies. We describe the structural features that determine Fe^{2+} translocation with atomistic detail, and we propose a putative mechanism for Fe^{2+} transport through the channel at the C3 symmetry axis, which is the only iron-permeable channel in vertebrate ferritins. Our findings have important implications for understanding how ion permeation occurs, and further how it may be controlled via purposely engineered channels for novel biomedical applications based on ferritin.

Twenty-four-mer ferritins are ubiquitous iron storage proteins that share a common architecture: a protein nanocage (see Fig. 1*A*) assembled from subunits made up by a 4-helix bundle (helices H1–H4) structure completed by a short C-terminal helix, H5, and a long loop connecting helices H2 and H3. This protein shell surrounds an 8-nm inner cage connected to the external environment by two different types of channels: eight channels in correspondence with the four 3-fold (C3, see Fig. 1*B*) symmetry axes and six channels in correspondence with the three 4-fold (C4, see Fig. 1*C*) symmetry axes of the octahedral point symmetry of the cage (1, 2). Despite many similarities across ferritins expressed in different species, the interiors of the C3 and C4 channels are quite variable, showing substantial differences in terms of hydrophobicity/hydrophilicity and electric charge distributions when comparing vertebrate ferritins with those from plants, bacteria, or archaea (3, 4). In turn, the specific chemical nature of these channels directly affects their transport properties and determines the preferred pathways followed by ferrous ions from the exterior of the cage to the catalytic ferroxidase center within the internal cavity. In vertebrate ferritins, for example, the C4 channels (about 12 Å in length) are relatively narrow and mainly hydrophobic, because of the residues belonging to the four H5 helices shaping the pore (5). On the other hand, the C3 channels (about 15 Å in length), which are formed by the N-terminal end of the H4 helices and the C-terminal end of the H3 helices, are wider and negatively charged (6, 7). As a result, only C3 channels are reported as viable pathways for ferrous iron uptake by vertebrate ferritins, whereas substitution of one or more channel residues may result in significant reduction of iron uptake and ferroxidase activity (8–11). Conversely, iron transit through the vertebrate C4 channels has been achieved by replacing neutral residues with negative ones at their bottom end, thus mimicking wild-type C3 channels (8). This experimental evidence has suggested that the presence of carboxylates at the inner edge of wild-type C3 channels, as well as engineered at the inner edge of C4 channels, determines a favorable electric field for driving Fe^{2+} into the cage. Accordingly, high-resolution X-ray crystal structures (12, 13) have shown two ferrous hexa-aqua ions within vertebrate C3 channels, but only one iron ion within the C4 channels coordinated by four His-169 Nϵ2, a water molecule, and a chloride anion (see Fig. 1*C*).

Nevertheless, many aspects concerning iron translocation through wild-type and mutant ferritin channels are not well understood. For example, it has to be confirmed whether Fe^{2+} ions do translocate as fully hydrated ions, as suggested by X-ray structures. A previous theoretical study (5) based on a continuous dielectric model predicted the presence of up to three iron

* This work was supported by the Ministero dell'Istruzione, dell'Università e della Ricerca (MIUR) through the PRIN program (Contract 2012SK7ASN). This work was also supported by a Scuola Normale Superiore Young Researchers Grant (2015/58) (to B. C.). The authors declare that they have no conflicts of interest with the contents of this article.

[S] This article contains supplemental Figs. S1–S5 and supplemental Table S1.

[1] To whom correspondence may be addressed. E-mail: bala.chandramouli@sns.it.

[2] To whom correspondence may be addressed. E-mail: giuseppe.brancato@sns.it.

ions within the wild-type C3 channel. However, this result partially contrasts recent experiments (12, 13). The effect of pore size in addition to electrostatics, the number of ions simultaneously permeating each channel, and the role of cooperativity for ion transport are other important aspects that require elucidation. Addressing the above questions is of paramount importance not only for understanding the natural function of these peculiar protein nanocages, but also for developing new strategies for the inclusion of imaging probes, drugs, and theranostic agents into ferritin-based nanocarriers. Indeed, in wild-type vertebrate ferritins, free diffusion through the cage is basically limited to water and small cationic ions that can enter the cage through the C3 channels (14, 15). Besides, modulation of channel hydrophilicity has been proposed to be a key factor for developing highly sensitive magnetic probes based on paramagnetic metal ions, because of the influence on water exchange with bulk (16, 17). For these reasons, a better understanding of the molecular basis of ion transport through ferritin channels may prove extremely useful to guide the design of specific mutants endowed with transport properties suited for tailored substrates, thus boosting the development of biologically inspired nanodevices to accomplish specific tasks exploiting new or enhanced functionalities.

Here, we present a thorough molecular dynamics study of the wild-type bullfrog *Rana catesbeiana* H′ ferritin, a well known model for vertebrate ferritins (18), and some of its channel variants that allow us to better assess, at atomistic level, the role of electrostatics and describe some aspects of the Fe^{2+} translocation process that are fundamental for ferritin biology. In particular, the C3 channel ferritin variants include a single mutant (E130A, hereafter referred to as C3SM)[3] and a triple mutant (D127A/E130A/S131A, hereafter referred to as C3TM), displaying a gradual increase of hydrophobic character of the pore; the C4 channel variant is a triple mutant (M161D/L165D/H169D, hereafter referred to as C4TM) that, conversely, introduces acidic residues into an otherwise mostly hydrophobic pore (see Ref. 8 for more details). Although some kinetic data on C3SM, C3TM, and C4TM were already available in the literature (8, 19), here, we directly compare, for the first time, their behavior during single and multiple catalytic cycles. Kinetic measurements of all the above variants, in which the iron inward flux is monitored by following the rate of formation of reaction intermediates at the ferroxidase center and ferric-precursors of the biomineral, furnish the experimental validation of our computational results. Altogether, these systems provide a suitable spectrum of ferritin channels for studying in some detail how iron transport occurs and to gain further insights on how to possibly control it.

Results

Structural Characteristics of the C3 Channel—The main structural features of the C3 channel, both native and mutant species, and the stability and solvent coordination of the permeating iron ions were investigated through extensive molecular dynamics simulations. In addition, we tested the effect of the presence and the absence of Fe^{2+} within the channel, because the X-ray crystal structure (Protein Data Bank (PDB) ID: 4MJY) displays two Fe^{2+} aqua ions occupying nearby sites in the channel interior (Fig. 1, *B* and *D*). The effect of mutation on the structural features of the C3 channel was examined by estimating the channel radius along a longitudinal direction (*i.e.* *Z*-coordinate; see supplemental Fig. S1).

In the wild-type C3 channel (C3WT), visual inspection revealed that both Fe^{2+} aqua ions remained stable in approximately the same sites observed in the crystal structure, throughout the simulation. On the contrary, in the single mutant system, only one Fe^{2+} aqua ion, initially located in the more internal site (*i.e.* closer to the cavity), was maintained, whereas the other was soon released into the environment. In the C3TM system, the triple alanine substitution resulted in the fast displacement of Fe^{2+} from both sites, because of the acquired hydrophobic character of this constricted region.

Some interesting features emerged from the comparative analysis of the C3 channel dimension in all considered systems. First, the profile of the channel radius along the pore of C3WT (Fig. 2, *A* and *A′*) showed noticeable differences in the absence or presence of Fe^{2+}, especially in the vicinity of the acidic residues (Asp-127 and Glu-130). In the absence of iron, the pore size was observed to have a larger variance than in the presence of the two iron ions. In the latter case, both the radius profile and the location of the two Fe^{2+} ions nicely matched those obtained from the X-ray structure (Fig. 2*A′*). In C3SM (Fig. 2, *B* and *B′*), the presence or absence of the single stable Fe^{2+} ion had a smaller influence on the channel dimension, which overall appeared wider than in wild type. In C3TM, the C3 channel is even wider than in the previous system, due to substitutions with the relatively smaller alanine residues. These results indicate that Asp-127 and Glu-130 alter their orientations in the presence of Fe^{2+} ions (supplemental Fig. S2).

Hydration of wild-type and mutant C3 channels was analyzed in terms of solvent density along the channel. In C3WT, the channel is well hydrated (Fig. 3, *A* and *A′*) and shows structured and stable water molecules coordinated by both Fe^{2+} ions (*i.e.* six water molecules around each ion). These results show that ferrous iron ions tend to retain their first solvation shell within the channel, in accordance with X-ray crystal structures (12, 13, 20). In C3SM, channel hydration was observed to change in the absence (Fig. 3*B*) and presence (Fig. 3*B′*) of Fe^{2+}, where in the latter case the channel is sparsely hydrated. However, at the internal Fe^{2+} site, a water cluster around the ion, similarly to the wild-type model, was observed. In C3TM, the channel is basically occluded to water, as expected, because of the substantial increase in channel hydrophobicity.

Fe^{2+} Localization within the C3 Channel—To characterize the binding sites of Fe^{2+} along the C3 channel, additional simulations of the C3WT and C3SM models were performed and the spatial occupancy of iron ions and carboxylic groups belonging to Asp-127 and Glu-130 was evaluated (Fig. 4). To this end, in some cases, we removed one or both Fe^{2+} ions within the ferritin channel from the initial configuration, and we allowed new Fe^{2+} ion entries from the solution, in contrast

[3] Throughout this study, the following designations are used for ferritin variants and wild type: C3SM, E130A single mutant; C3TM, D127A/E130A/S131A triple mutant; C4TM, M161D/L165D/H169D triple mutant; C3WT, wild-type C3 channel; C4WT, wild-type C4 channel.

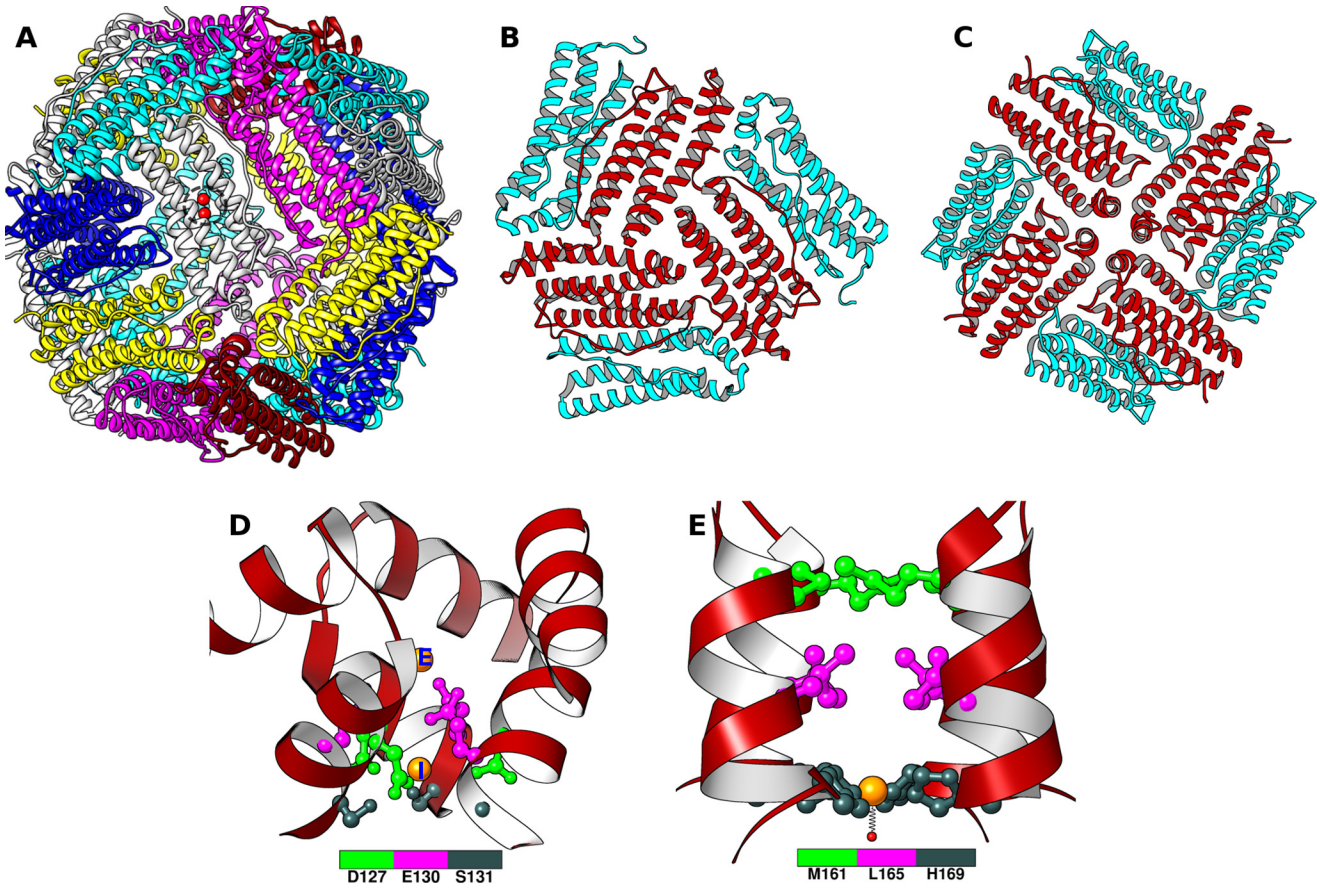

FIGURE 1. **Ferritin structural elements.** *A*, X-ray crystal structure of frog H′ ferritin (PDB ID: 4MJY). One of the ferroxidase cavities, with irons bound to the dinuclear catalytic site, is *circled*. *B* and *C*, three-dimensional arrangement of the C3 (*B*) and C4 (*C*) channels. *D* and *E*, magnified views of C3 (*D*) and C4 (*E*) channels. Residues subjected to mutation are shown as colored balls and sticks, Fe^{2+} ions within the channel, as observed in the X-ray structure, are in *orange*, and water oxygen is in *red*.

to previous simulations where external Fe^{2+} ion positions were kept frozen. In all cases, we observed that, when present, Fe^{2+} is firmly bound as a hexa-aqua ion in correspondence with acidic residues, and hence, well localized within the channel. As a result, we could not observe the spontaneous release or translocation of Fe^{2+}, once inserted into the C3WT or C3SM system. In the C3WT model, the distribution of iron occupancy matched well the positions observed in the X-ray structure (Fig. 4*A*), with the Fe^{2+} ion located farther from the cavity, only slightly shifted with respect to its crystal position. On average, the iron-iron distance was about 6.25 Å. When the Fe^{2+} ion at the more internal site was removed, thus leaving only one ion in the channel, a further inward shift (~0.4 Å) in the average position of the externally located Fe^{2+} was observed (Fig. 4*A*′). Interestingly, when additional iron ions were added to the bulk solution and left free to move, one Fe^{2+} ion was found to occupy the internal site, thus restoring the previous crystal-like arrangement of two Fe^{2+} ions (Fig. 4*A*″). In C3SM, structural fluctuations in the spatial distribution of the carboxylic group of Asp-127 were observed as a result of E130A mutation (Fig. 4*B*), and concurrently, there was a downward shift in the location of Fe^{2+} at the internal site as compared with the wild-type channel. When the C3SM channel was initially cleared from Fe^{2+}, a new iron ion was found to occupy the same internal site after ~15 ns, reproducing very similar spatial distributions (Fig. 4*B*′). In summary, our simulations revealed the strong preference for two Fe^{2+} ions by the wild-type C3 channel and only one Fe^{2+} in the case of the single mutant, whereas the triple mutant channel displayed no Fe^{2+} inside. Moreover, the locations of iron aqua ions along the C3 channel were shown to be sensitive to mutations, thus providing important insights to interpret functional studies and to define structural mechanisms for iron uptake.

Structural Characteristics of the C4 Channel—The channel radius along the wild-type C4 (C4WT) model showed a narrower profile (Fig. 5) with respect to the C3 channel. This was expected because the side chains of the residues shaping the channel (Met-161, Leu-165, and His-169) are mostly projected toward the channel center (Fig. 1*E*) because of favorable hydrophobic interactions. As a result, the channel appeared overall constricted. The crystallographic Fe^{2+} ion, initially coordinated by His-169, was soon displaced into the solution in our simulation. In the crystal structure, Fe^{2+} is also coordinated by a chloride ion, which is absent in our simulations (see "Experimental Procedures"). In the triple mutant (C4TM), substitutions with negatively charged aspartates significantly increased the channel dimension (Fig. 5), as a consequence of charge-charge repulsion. Besides, the spontaneous entry of one Fe^{2+} into the channel from the exterior vestibule confirmed that iron uptake is triggered by electrostatic effects. As described in the

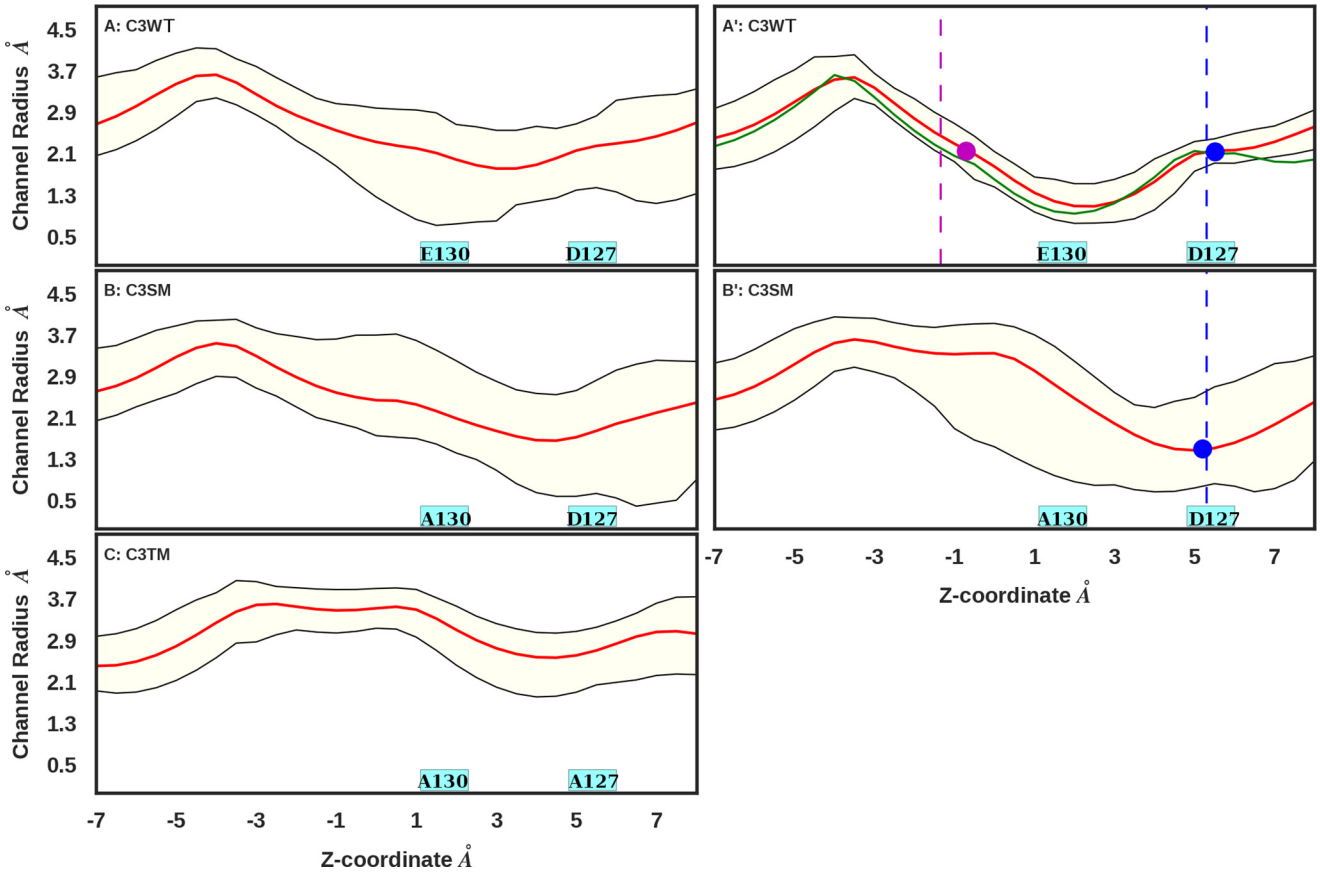

FIGURE 2. **C3 channel dimension analysis.** Shown is a profile of the channel radius along the C3 channel (*i.e. Z*-coordinate). *Black lines* represent the minimum and maximum observed radius size, whereas the *red line* is the average. In *panels A*, *B*, and *C*, simulations with no Fe^{2+} ions in the channel. In *panels A′* and *B′*, simulations with Fe^{2+} ions in the channel; the average Fe^{2+} ion positions are represented as *colored dots*. In *panel A′*, the *green line* is the radius size as observed in the X-ray structure, and in panels *A′* and *B′*, the *vertical dashed lines* are Fe^{2+} ion positions as observed in the X-ray structure.

Introduction, recent experimental results demonstrated iron uptake in the triple mutant C4 channel, after switching off the uptake via the C3 channel (8). Hydration of wild-type and mutant C4 channels showed a marked difference in water density along the channel (Fig. 6). In the wild-type model, the C4 channel was void of water molecules due to the highly hydrophobic environment and constricted space. On the other hand, the introduction of negatively charged residues led to a densely hydrated C4 channel, and the larger available space permitted the intake of the ferrous iron with its full solvation shell (Fig. 6).

Free Energy Barriers for Iron Translocation through C3 and C4 Channels—Free energy barriers for the translocation of a single Fe^{2+} ion through wild-type and mutant C3 and C4 channels were evaluated by computing the potential of mean force (PMF).[4] The Fe^{2+} position along the channel axis (*i.e. Z*-coordinate) was adopted as the PMF coordinate (supplemental Fig. S1). The PMF profile for the wild-type C3 model (C3WT) showed a first local minimum at $Z = -0.5$ Å, as proceeding from the outer environment toward the ferritin cavity, and a global minimum at $Z = 5.3$ Å (Fig. 7), in perfect correspondence with the favorable Fe^{2+} locations previously identified. Indeed, the spatial occupancies of Fe^{2+} ions obtained from the C3WT simulation are exactly distributed around the computed PMF minima. The two minima are separated by an energy barrier (about 5 kcal/mol) located around $Z = 1.0$ Å inward with respect to the external binding site (Fig. 7). This corresponds to position Glu-130 along the channel, and we noted that such an energetic cost arose from the loss of one water molecule, from six to about five, within the first hydration shell of Fe^{2+} (supplemental Fig. S3), only partially compensated by Coulomb interactions with the negatively charged glutamate ring. As expected, the PMF profile revealed a strong attractive character of the C3 channel interior for ferrous iron (escaping barriers are >15 kcal/mol). In C3SM, the overall PMF profile appeared flattened, with the exception of a noticeable energy barrier in correspondence with the mutation site (*i.e.* E130A; $1 < Z < 2$), where the PMF resulted in an increase of about 15 kcal/mol as compared with the wild-type channel. Afterward, a gradual PMF downhill is observed. Such a large barrier explains the displacement of Fe^{2+} from the external site in C3SM simulation, upon the loss of the favorable electrostatics. In the C3TM model, the PMF displayed a very repulsive barrier for the iron ion approaching the channel center; therefore, an opposite scenario could be predicted for iron uptake with respect to the wild-type channel. Conversion of the negatively charged residues into hydrophobic ones made the C3 channel rather impermeable to ions, thus leading to the total displacement of Fe^{2+} from the channel. These results are in good agreement with the experimental evidence on the influence of mutations on iron

[4] The abbreviations used are: PMF, potential of mean force; DFP, diferric-peroxo; DFO(H), diferric-oxo/hydroxo.

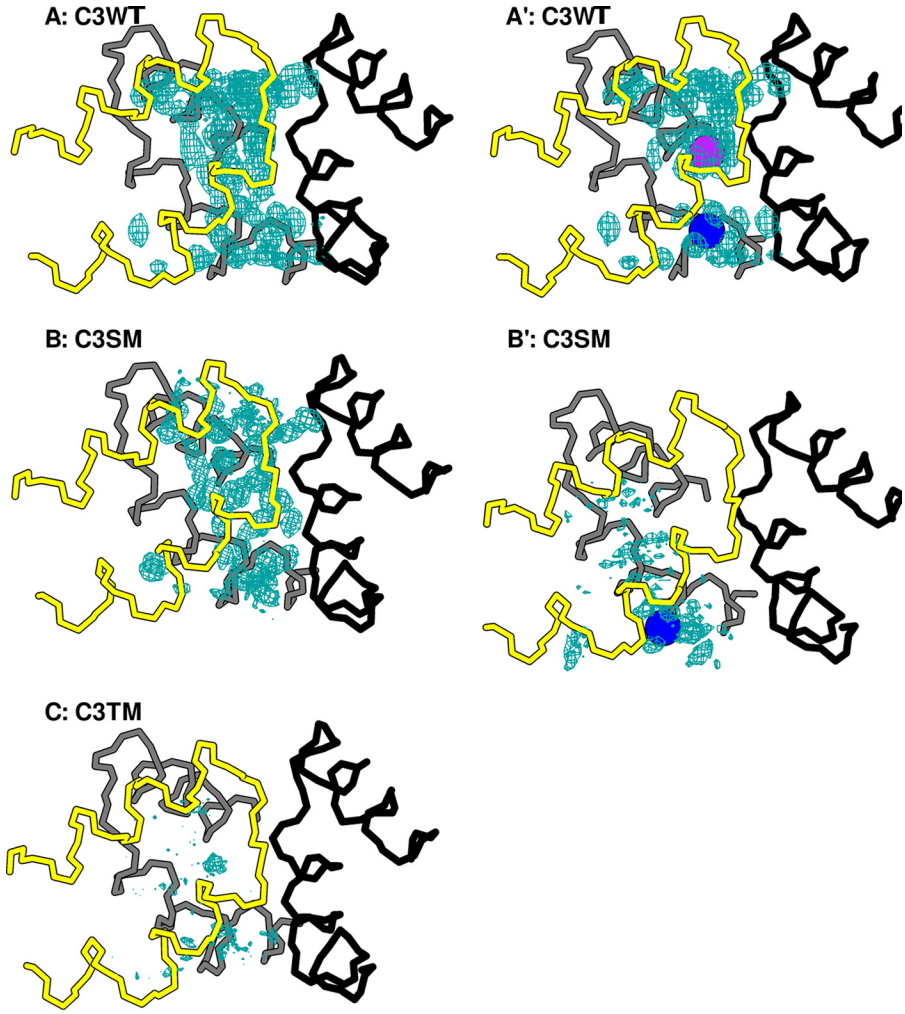

FIGURE 3. **C3 channel hydration analysis.** Shown is the density of water molecules along the C3 channel. The *left panels* depict the channel hydration in the absence of Fe^{2+}. The *right panels* depict the channel hydration in the presence of Fe^{2+} ions. Individual ferritin subunits constituting the channel are colored differently. Fe^{2+} ions are shown as *colored spheres*.

uptake (8). In both variants (*i.e.* C3SM and C3TM), Fe^{2+} maintained its full hydration layer (supplemental Fig. S3) while moving inside the channel (*i.e.* six water molecules), consistently to a larger pore radius (Fig. 2).

In C4WT, the barrier for ion translocation is extremely high (Fig. 7) because the wild-type C4 channel is spanned by hydrophobic residues. Hence, iron uptake is unlikely to occur through this pathway, in agreement with experimental findings (8, 12). On the contrary, in the triple mutant (C4TM), substitutions with aspartates enabled strong electrostatic interactions and a wider pore than wild type, thus favoring Fe^{2+} hexa-aqua ion translocation.

Despite the favorable PMF profile of C3WT, one may wonder whether Fe^{2+} transport rate could be enhanced by any sort of ion cooperativity effect, considering the deep energy minima characterizing the two ferrous iron sites as observed above. To this end, we have tested experimentally the possible role of Fe^{2+} concentration on iron uptake, as reported below.

Kinetic Analysis of Iron Uptake of Ferritin Variants versus Wild Type—From an experimental point of view, the efficiency of iron transit through ferritin channels can be monitored by measuring the kinetics of the catalytic oxidation reaction occurring at the ferroxidase sites within the cavity. In fact, hindered iron translocation results in an inefficient delivery of the Fe^{2+} substrate to the ferroxidase sites and therefore into an inhibited catalytic reaction. The catalytic reaction can be monitored through the formation of transient diferric-peroxo (DFP) intermediates, with maximum absorbance at 650 nm, and diferric-oxo/hydroxo (DFO(H)) species, precursors of the biomineral, that absorb at 350 nm (21). In the case of the C3 channel, single-turnover catalysis (2 Fe^{2+}/subunit) was progressively quenched upon substitution of the carboxylate residues, as demonstrated by the data reported in Fig. 8, where the rate of formation of the DFP and DFO(H) species decreases in the order WT > E130A > D127A/E130A/S131A.

It is reported that, at a high Fe^{2+}/cage ratio in WT cages, a slower direct oxidation of ferrous ions on the surface of the biomineral core adds to the fast enzymatic oxidation at the ferroxidase center (3). Transit through the channels is obviously expected to also modulate the rate of oxidation at the biomineral surface. Here, experiments with a higher Fe^{2+}/subunit ratio (namely, 20 Fe^{2+}/subunit) were performed (Fig. 9). Under these conditions of multiple ferroxidase turnover and possible biomineral surface self-oxidation, the overall reaction

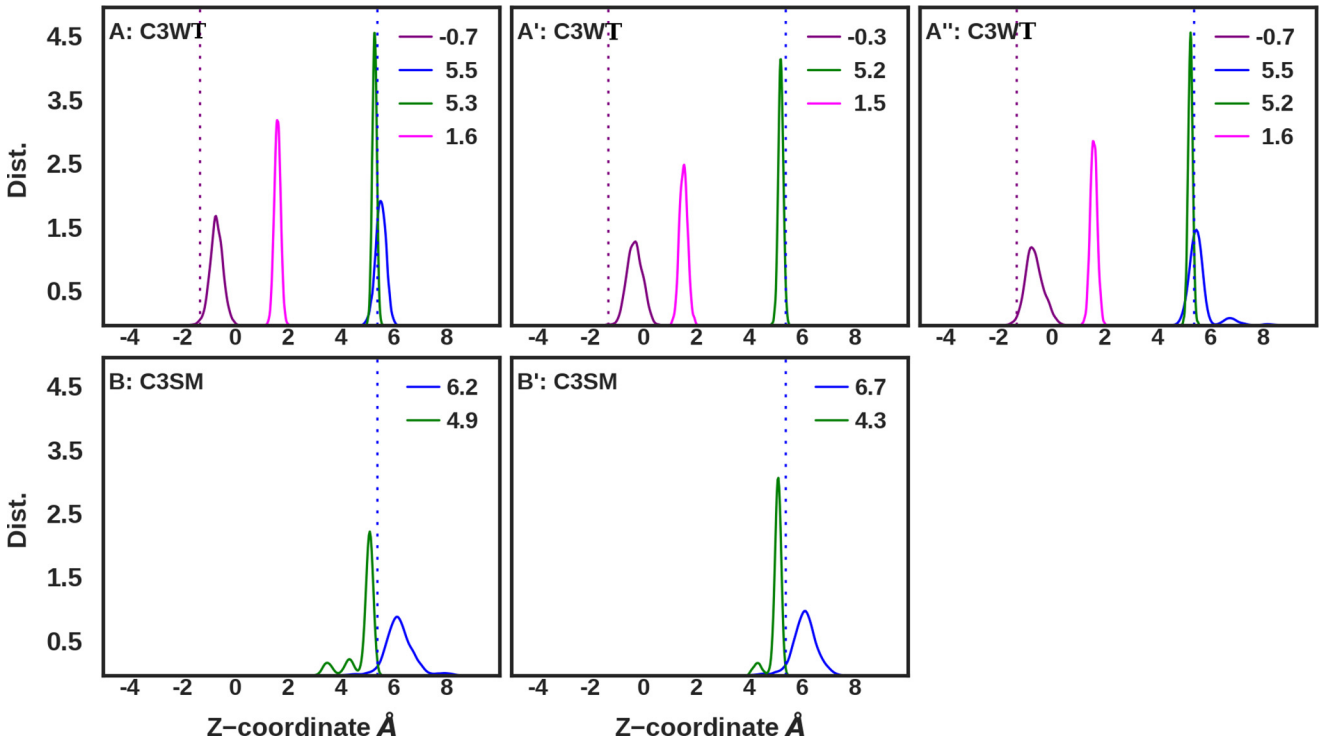

FIGURE 4. **Fe^{2+} ions and protein carboxylic groups localization.** Shown is the spatial occupancy of Fe^{2+} ions and protein carboxylic groups along the C3 channel pathway in C3WT (*A–A″*) and C3SM (*B*, *B′*). *A*, Fe^{2+} ions at the external site (*purple*), internal site (*blue*), C_γ centroid of Asp-127 (*green*), and C_δ centroid of Glu-130 (*magenta*). *Dist.*, distribution. *A′*, simulation initiated after moving Fe^{2+} ions at the internal site into the bulk. *A″*, simulation initiated with increased concentration of bulk Fe^{2+} ions. *B*, Fe^{2+} ions at internal site (*blue*) and C_γ centroid of Asp-127 (*green*). *B′*, simulation initiated after moving Fe^{2+} ion in the internal site into the bulk. The *dotted lines* represent the position of Fe^{2+} ion in the X-ray structure of the WT protein.

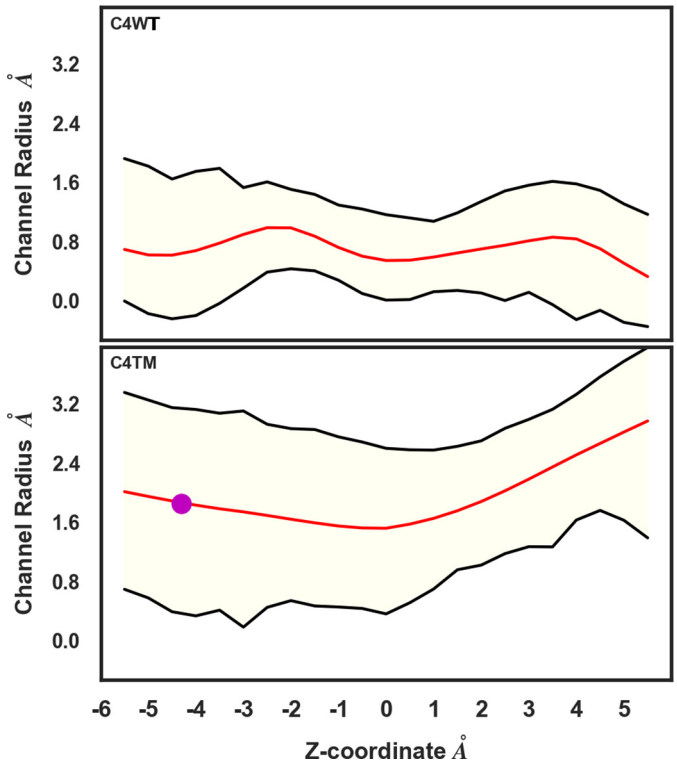

FIGURE 5. **C4 channel dimension analysis.** The channel radius profile is shown as a function of *Z*-coordinate. Data represent the minimum and maximum radius values (*black lines*) along with the time average (*red line*). The *filled circle* indicates the average position of the Fe^{2+} ion that entered the mutant C4 channel during the dynamics.

rate in the C3TM is drastically reduced (down to ~30%) with respect to C3WT, whereas the effect in the C3SM is relatively small (~70%). This observation appears in very good agreement with free energy calculations reported above.

In addition, other studies have reported the possible interaction of metal ions with Cys-126 residues located at the entrance of C3 channels (22), and the interaction with Fe^{2+} has also been inferred (23). Our data (supplemental Figs. S4 and S5) clearly showed that there are no significant differences in the reaction rates measured with 2 Fe^{2+}/subunit nor with 20 Fe^{2+}/subunit, upon C126A mutation. As a consequence, we may conclude that iron uptake is not significantly assisted by Cys-126.

Discussion

Our *in silico* study fully supports recent high-resolution X-ray structures that demonstrated a doubly occupied native C3 channel by iron hexa-aqua ions (*i.e. R. catesbeiana* H′ ferritin (12) and human H ferritin (13)). By enabling thermal fluctuations and the surrounding aqueous environment in our simulations, we observe that the two hydrated Fe^{2+} ions are firmly bound within the 3-fold channel by forming favorable electrostatic interactions with negatively charged side chains (*i.e.* Asp-127 and Glu-130), while keeping the same microsolvation observed in the crystal. Not only does such a molecular configuration reproduce the experimentally resolved structures fairly well, but it also provides a possible key step for deciphering the iron uptake mechanism, as discussed below. Our atomistic simulations suggest that the channel size and length do not allow the stable binding of additional iron ions with respect to those

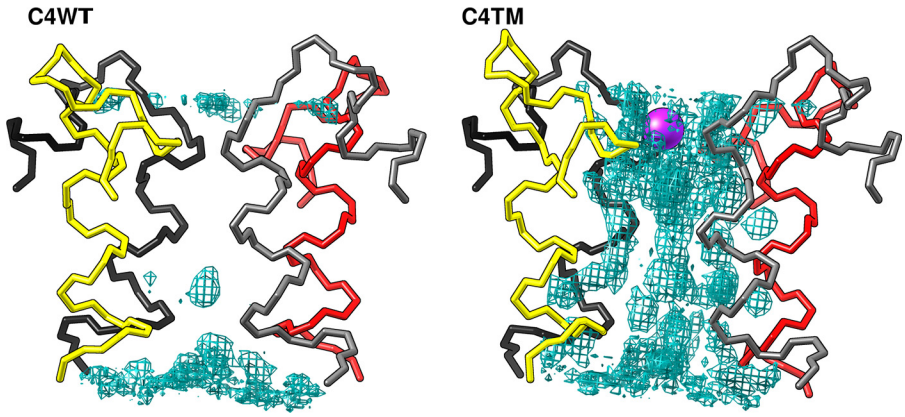

FIGURE 6. **C4 channel hydration analysis.** Shown is the grid density of water molecules along the C4 channel. The four individual subunits constituting the channel are colored differently. The *purple sphere* indicates the Fe^{2+} ion.

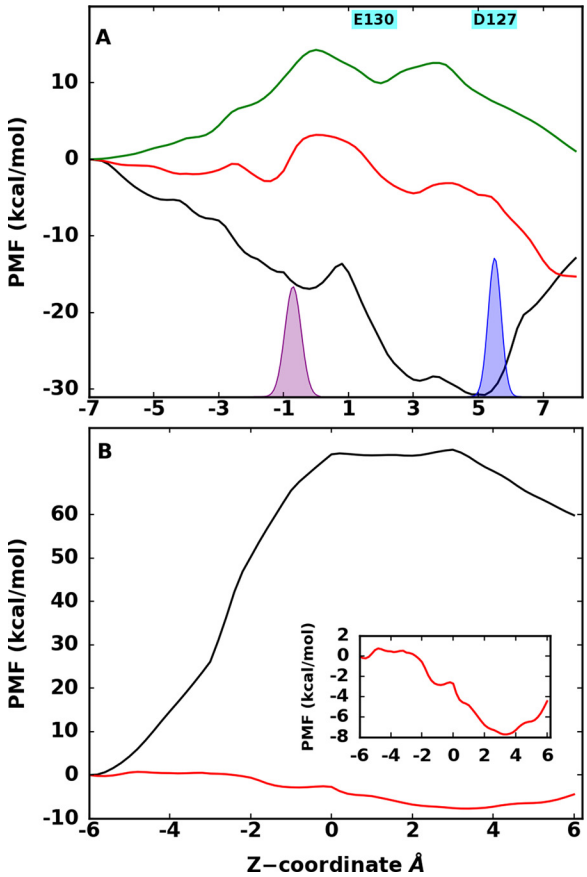

FIGURE 7. **Free energy of Fe^{2+} translocation.** *A* and *B*, free energy profiles for single Fe^{2+} ion translocation through C3 (*A*) and C4 (*B*) channels. *A*, data for C3WT, C3SM, and C3TM are shown in *black*, *red*, and *green*, respectively. The distribution shows the spatial occupancy of Fe^{2+} ions at external and internal sites in the C3WT model. *B*, data for C4WT and C4TM are shown in *black* and *red*. The *inset plot* depicts an enlarged view of the PMF profile for the C4TM system.

found in the crystal, in contrast to a previous theoretical study (5) reporting up to three iron ions within the wild-type C3 channel, which probably resulted because of the lack of atomistic detail in that study.

On the other hand, we confirm the crucial role played by electrostatics in modulating the transport properties of ferritin channels. Concerning the wild-type C3 and C4 channels, as found in vertebrate ferritins, the computed free energy profiles of Fe^{2+} translocation provide a thermodynamic ground to understand why only the C3 channel represents a viable iron entryway, as already proposed on the basis of mutagenesis studies involving residues inside the C3 channels (3). Here, the progressive introduction of hydrophobic residues into the C3 channel lumen, as obtained in the E130A and D127A/E130A/S131A ferritin variants, is reflected into a steep rise of the energy barrier against Fe^{2+} transit, a result consistently validated by our kinetic experiments following iron catalytic oxidation. It is worth noting that, from the structural viewpoint, substitutions by alanine lead to an overall increase of C3 pore size, because of the less bulky side chains. However, the augmented pore dimension does not compensate for the loss of favorable electrostatic interactions. A similar picture is confirmed when, conversely, charged residues are introduced in the mostly hydrophobic C4 channel, as obtained going from the wild type to the triple mutant (C4TM).

Moreover, we notice a close correlation between hydrophobicity and solvent density within the channels, even in the absence of any iron ion. This result appears as another manifestation of how ion permeation through constricted channels may be modulated by the formation/disruption of hydrophobic interactions, a well known effect already described in the context of membrane protein channels (24–27). Interestingly, our simulations indicate that Fe^{2+} transit into wild-type C3 and triple mutant C4 (C4TM) channels occurs basically as an almost fully hydrated ionic species (*i.e.* hexa-aqua ion); in the case of C3WT, only one water molecule is lost while passing through the most constricted region of the pore. These results, although they have to be considered with caution due to inherent approximations in our modeling, do support the view that ferrous iron does travel as aqua ions from the outer environment to the ferroxidase catalytic centers within the ferritin cage, as observed in X-ray crystal structures. Additionally, the present kinetics data exclude any involvement of Cys-126, a solvent-exposed residue located on the ferritin shell close to the C3 channel entrance, in the iron uptake process, contrary to previous suggestions (23). Concerning the 4-fold channel, the larger number of negative charges and the wider pore size of C4TM with respect to C3WT account for the higher iron uptake rate observed in the former ferritin variant (8).

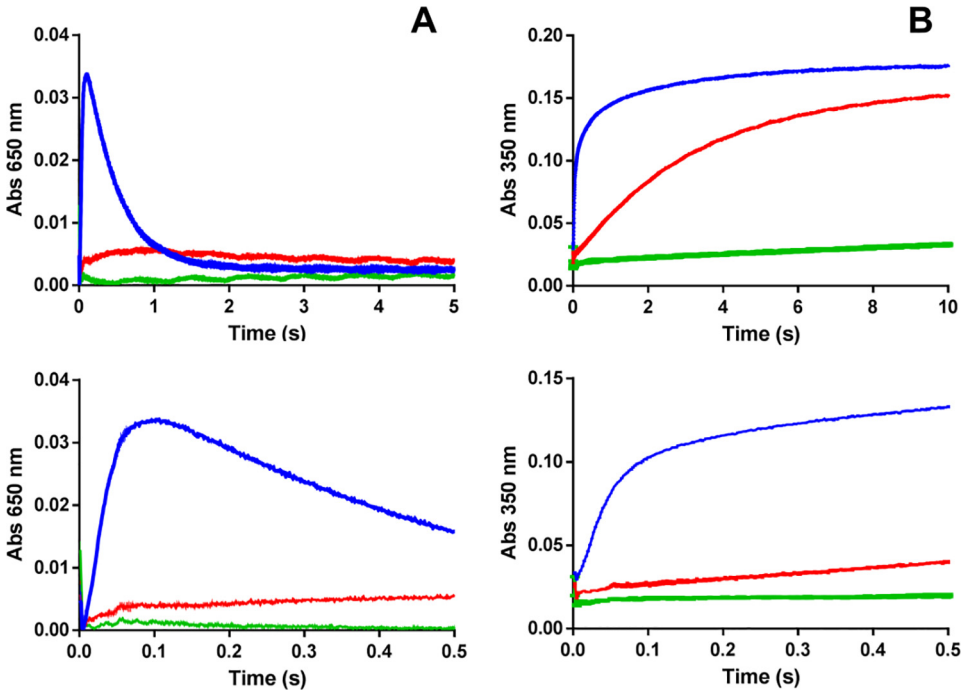

FIGURE 8. **Iron uptake rate measurements at 2 Fe^{2+}/subunit ratio.** The C3 channel properties modulate activity in structurally intact ferritin cage variants. *A* and *B*, formation of DFP intermediate ($A_{650\ nm}$) (*A*) and DFO(H) ($A_{350\ nm}$) (*B*) products after the addition of 2 Fe^{2+}/subunit to wild-type (*blue*), C3SM (*red*), and C3TM (*green*) variants. The *lower panels* show enlargements of the first 0.5 s to highlight the differences in the initial rates. Shown is a set of curves (mean ± S.D.) of a representative experiment from at least three experiments, each one performed in triplicate. *Abs*, absorbance.

Furthermore, our free energy analysis provides evidence that can be recast in terms of mechanistic prescriptions for iron translocation. In particular, the single-ion potential of mean force highlights the presence of two favorable binding sites for iron aqua ions along the C3 channel. These sites are in good agreement with Fe^{2+} localization in the doubly occupied channel, as observed in equilibrium molecular dynamics simulations and crystal structures. However, the escaping potentials from these local energy minima do appear incompatible with an effective "single-ion" translocation process. Therefore, we posit that a "multi-ion" cooperative effect takes place by smoothing out these energy barriers, thus favoring the flow of Fe^{2+} ions along the channel, in analogy to what has been observed in other well known biochannels (*e.g.* voltage-dependent K^+ channels (28)). In support of this hypothesis, we observe a non-linear increase of the initial rate of DFP formation at an increasing Fe^{2+}/subunit ratio in wild-type ferritin (Figs. 8 and 9). Such a non-linear trend can easily be rationalized if one takes into consideration the possibility of two different ion transport mechanisms at low and high Fe^{2+}/subunit ratios, with a multi-ion mechanism being activated at a high Fe^{2+}/subunit ratio. This multi-ion mechanism would also explain the apparently counterintuitive kinetics data recently reported (8) on a ferritin variant equipped with all active channels (*i.e.* eight C3WT and six C4TM channels) at low Fe^{2+}/subunit ratios: the rates of reaction as well as the total amount of formed products with 2 Fe^{2+}/subunit dropped to 30% of wild-type values (*i.e.* eight C3WT and six C4WT channels) and about 5% of C3TM/C4TM variant (*i.e.* eight C3TM and six C4TM channels), whereas with 4 Fe^{2+}/subunit, the initial reaction rate was 1.5 times faster than in the wild-type ferritin. Altogether, these results support the view that a minimum number of iron ions are needed in each ferritin channel to enable an efficient ionic flow, thus suggesting a "functional" role for the doubly occupied C3 channel configuration. One might speculate that the need of multiple iron ions to activate the metal transport across the channels reflects the biological need to initiate biomineralization only at high iron concentrations.

Indeed, as a further step toward a complete understanding of Fe^{2+} transport through the wild-type C3 channel, we postulate a simple translocation mechanism that cyclically involves this intermediate configuration, observed via X-ray crystallography, and that consists of an alternating sequence of a doubly occupied (2 Fe^{2+} ions) state and a singly occupied (1 Fe^{2+} ion) channel intermediate state, as illustrated in Scheme 1 (*Pathway A*). One may also envisage a putative mechanism in which iron ions displace one another in a concerted fashion, as if pushed by an entering Fe^{2+} ion (Scheme 1, *Pathway B*), as suggested in a previous study (29). However, test simulations aiming to reproduce the latter scenario provided an unsatisfactory outcome, showing no ion displacement in response to a Fe^{2+} ion being pulled from the outer environment into the channel. Nonetheless, more information is required to fully demonstrate the translocation mechanism followed by Fe^{2+} aqua ions (for example, the possible role of negative counterions in assisting iron passage from the ferritin channels into the cavity), and some questions still remain open. Accordingly, we believe that a key factor to understand what drives the iron translocation process is represented by the exact, but yet unknown, electrochemical conditions at which it operates within the cellular environment.

Finally, the present study highlights the versatility of ferritin channels to achieve desirable transport properties. This property is particularly relevant for those nano-biotechnological

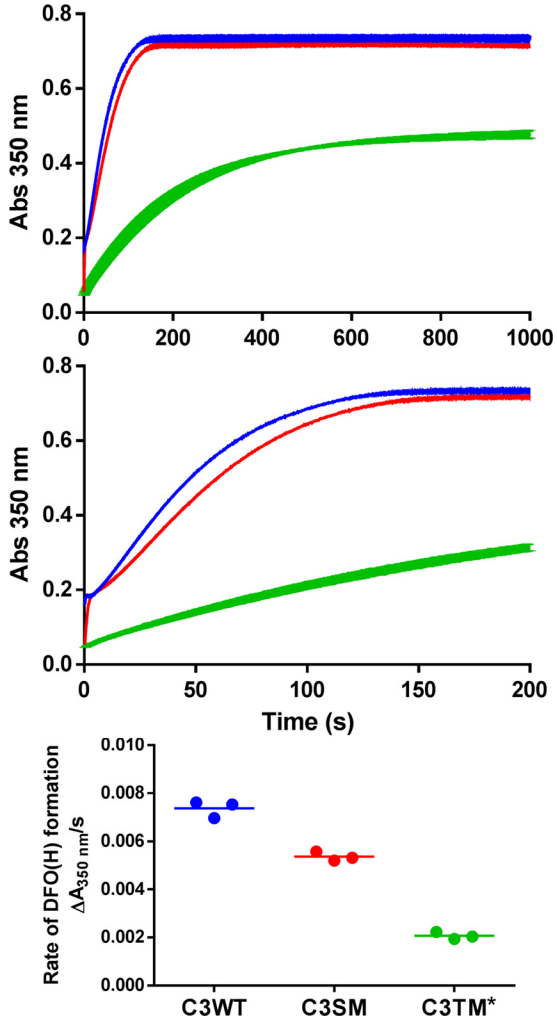

FIGURE 9. **Iron uptake rate measurements at 20 Fe^{2+}/subunit ratio.** *Top*, reaction progress at a high iron:protein ratio (20 Fe^{2+}/subunit; 480 Fe^{2+}/cage) in wild-type (*blue*), C3SM (*red*), and C3TM (*green*) variants monitored as DFO(H) product ($A_{350\ nm}$) formation. The *central panel* shows an enlargement of the first 200 s. *Upper* and *lower panels*, a set of curves (mean ± S.D.) of a representative experiment of at least three (*upper panels*), each one performed in triplicate, and the corresponding scatter plots of the average initial rates (*lower panel*). *, significantly different from the corresponding value in wild type; $p < 0.05$. *Abs*, absorbance.

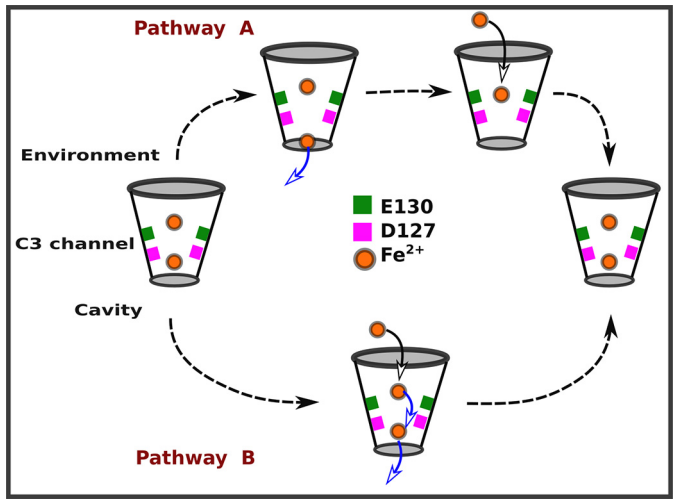

SCHEME 1. **Fe^{2+} translocation mechanisms through the C3 channel.** Shown are putative translocation mechanisms of Fe^{2+} through the wild-type C3 ferritin channel. In *Pathway A*, singly and doubly occupied channel states alternate with each other. Starting from the doubly occupied state, one Fe^{2+} ion is released into the cavity from the channel, dragged by an electrochemical gradient, and the remaining Fe^{2+} ion is shifted inward, leading to the singly occupied intermediate. Then, a new Fe^{2+} ion is introduced into the channel from the environment, thus restoring the initial state. In *Pathway B*, Fe^{2+} ions displace one another inwardly, as pushed by one Fe^{2+} entry. When tested in simulation, such a mechanism proved to be unfeasible, and no ion displacement occurred even if the entry ion was subject to an unrealistically large pulling force.

applications (14) where encapsulation of non-natural agents, such as molecules, metal particles, or ionic species, into the ferritin interior is realized through diffusion, eventually followed by intra-cage synthesis or self-assembly, but not through the disassembly and reassembly of the ferritin cage itself. In this regard, purposely engineered channels may favor or block molecular transport into ferritin by playing with suitable steric and electrostatic effects. As an example, an ion selectivity filter, such as those commonly found in ion-selective membrane channels, can be re-created into the ferritin channels to allow the specific uptake of given ionic species from bulk solutions. This idea may be coupled with current strategies for the direct mineralization of nanoscale materials inside the intact cage (14), thus achieving a high control of both particle size and nature. The same approach could be perhaps exploited to sequester given ionic species from solutions where multiple salts are dissolved, with the purpose, for example, of recovering noble and precious metal ions. Another interesting possibility would be to embed within the ferritin cage a pH probe to monitor the local acidity of the environment, especially in cell imaging applications. To this end, one may think to assess the exchange rate of protonated water as a function of channel characteristics. Interestingly, one may envisage the introduction of light-activated and controllable gating mechanisms, such as those that have been employed in various membrane channel applications (30, 31). In conclusion, our study provides a successful example of a computational approach that can be employed for the design of ferritin nanocages for novel biomedical or nano-technological applications in which the permeation or release of ionic species could be modulated at will through modeling-aided protein engineering.

Experimental Procedures

Molecular Dynamics Simulations—High-resolution X-ray crystallographic structures of *R. catesbeiana* H′ ferritin have recently been resolved at different time intervals after exposing the ferritin crystals to ferrous salt (12). Among others, the structure of the H54Q mutant (PDB ID: 4MJY), resolved after 60 min of exposure time, was selected to model the ferritin protein channels. This choice was motivated by the better resolution of Fe^{2+} aqua ions within the C3 channel in this structure with respect to the wild-type structure, even if C3 and C4 channel residues are basically identical in the two cases. Then, Gln-54 was substituted with histidine to model the wild-type protein. To reduce the computational cost, the starting models for the C3WT and C4WT channels were generated by considering only the subunits that constitute the channel pathway and immediate neighboring subunits, which give rise to subunit dimers via extended surface contacts along C2 symmetry axes,

as shown in Fig. 1, *B* and *C*. Starting structures were immersed in an orthogonal TIP3P water box that extended up to 14 Å from the protein van der Waals surface. In the C3WT system, Fe^{2+} aqua ions located in the C3 channel (Fig. 1*D*) were retained, and in the C4WT system, the iron-aqueous adduct at the internal vestibule of the C4 channel (Fig. 1*E*) was retained. Further, ferrous iron ions bound at the ferroxidase sites of the subunits were retained. Other crystallographic ionic species were removed (*e.g.* Cl^-). Finally, Na^+ ions were added to ensure system electroneutrality. All simulations were carried out with the NAMD program (version 2.10), using the Amber ff14SB force field for protein and CM parameters for iron (32, 33). Starting systems were equilibrated following a multi-step protocol: (i) two rounds of minimizations (6000 iterations) and dynamics (300 ps, $\Delta t = 1$ fs) of water molecules and Na^+ ions in the bulk, keeping the protein and iron ions restrained ($k = 2$ kcal/mol Å^2), (ii) minimization of the whole system (15,000 iterations), (iii) heating up to 303 K in the NVT ensemble (500 ps, $\Delta t = 1$ fs), and (iv) final equilibration in the NPT ensemble (2 ns, $\Delta t = 2$ fs). The production phase was then initiated, during which a mild restraining potential ($k = 0.5$ kcal/mol Å^2) was applied to C_α atoms of residues beyond 30 Å from the geometric centroid of C3/C4 channels to preserve overall topological symmetry. Snapshots were collected at intervals of 10 ps. Simulation settings included periodic boundary conditions, 2-fs time step for numerical integration, 12 Å cut-off for non-bonded interactions using a switching function from 10 to 12 Å, constraining bonds involving hydrogens with SHAKE (34), estimation of long-range electrostatics using the particle mesh Ewald (35) method, and temperature regulation with Langevin coupling using a collision frequency of 1.0 ps^{-1} (36). Simulations of the C3SM, C3TM, and C4TM systems were started from an equilibrated snapshot (~10 ns) of the corresponding wild-type systems after introducing the mutations *in silico*. The solvent environment was retained in all cases to avoid extensive re-equilibration. A summary of the simulated models is reported in supplemental Table S1. A further test simulation was carried out in which a Fe^{2+} ion was pulled from the outer environment into the C3WT channel to study its effect on the Fe^{2+} aqua ions located in the C3 channel (a Fe^{2+} ion was pulled for about 20 Å along the C3 channel to reach the internal cavity using a rate of 2 Å/ns and a spring force constant of 5 kcal/mol Å^2). Trajectories were analyzed with the HOLE program (37) and in-house codes written using the MDAnalysis library (38). Channel radius was estimated considering only the heavy atoms of residues shaping the pore. Figures and graphs were generated with the UCSF-chimera (39) and matplotlib (40) software.

Free Energy Calculations—The PMF profile for the translocation of Fe^{2+} ion along C3 and C4 channels was estimated using adaptive biasing force simulation methodology (41, 42). The method estimates the average force on a testing particle along a predefined transition coordinate (ξ). The average force is collected in bins along ξ and updated during the simulation. An adaptive biasing potential, equivalent and opposite to the average force, is applied after a defined number of samples in a bin to overcome any barrier along ξ. Herein, the PMF profile for a single Fe^{2+} ion translocation was estimated along the channel axis *i.e.* *Z*-coordinate (supplemental Fig. S1). Other Fe^{2+} and Na^+ ions in the bulk were restrained to avoid their entry into the channel. For C3 systems, adaptative biasing force simulations were performed in five windows of 3 Å length and 0.2 Å bin size, covering the full channel length of 15 Å. For C4 systems, four windows of 3 Å length and 0.2 Å bin size, spanning a total length of 12 Å, were used. The biasing potential was applied after 800 samples. The starting snapshot for each window was extracted from the preceding ones to mimic sampling in overlapping windows. Simulation for each window was carried out for 25 ns.

Mutagenesis—Site-directed amino acid substitution in *R. catesbeiana* H′ ferritin protein cages was generated by PCR, with expression plasmid pET-3a *R. catesbeian*a H′ ferritin DNA as template, using the QuikChange II site-directed mutagenesis kit (Stratagene). The DNA in the coding regions in all the protein expression vectors was analyzed for sequence confirmation (Primm Srl, Milan, Italy).

Protein Expression—pET-3a constructs encoding *R. catesbeiana* H′ WT ferritin and its variants were transformed into *Escherichia coli* BL21(DE3) pLysS cells, which were subsequently cultured in LB medium containing ampicillin (0.1 mg/ml) and chloramphenicol (34 μg/ml). Cells were grown at 37 °C, until $A_{600\ nm}$ reached 0.6–0.8, and subsequently induced with isopropyl 1-thio-β-D-galactopyranoside (1 mM final concentration) for 4 h. Recombinant ferritins were purified from the harvested cells, as described previously (43). Briefly, cells were sonicated, and the cell-free extract obtained after centrifugation (40 min, 40,000 rpm, 4 °C) was incubated for 15 min at 65 °C as the first purification step. After removal of the aggregated proteins (15 min, 40,000 rpm, 4 °C), the supernatant solution was dialyzed against 20 mM Tris-HCl, pH 7.5; applied to a Q-Sepharose column in the same buffer; and eluted with a linear NaCl gradient of 0–1 M in Tris 20 mM, pH7.5. Fractions containing ferritin, identified by Coomassie Brilliant Blue staining of SDS-PAGE gels, were combined and further purified by size exclusion chromatography using a Superdex 200 HiLoad 16/60 column. All variants had wild-type elution patterns.

Stopped-flow Kinetics—Single-turnover catalysis (48 Fe^{2+} ions per ferritin cage, two Fe^{2+} ions per subunit), in *R. catesbeiana* H′ ferritin, wild type or with amino acid substitutions, was monitored as the change in A_{650} nm (DFP) or $A_{350\ nm}$ (DFO(H)) after rapid mixing (less than 10 ms) of equal volumes of 100 μM protein subunits (4.16 μM protein cages) in 200 mM MOPS, 200 mM NaCl, pH 7.0, with freshly prepared solutions of 200 μM ferrous sulfate in 1 mM HCl in a UV-visible stopped-flow spectrophotometer (SX.18MV stopped-flow reaction analyzer, Applied Photophysics, Leatherhead, UK). Routinely, 4000 data points were collected during the first 10 s. Initial rates of DFP and DFO(H) species formation were determined from the linear fitting of the initial phases of the 650- and 350-nm traces (0.01–0.03 s). The reaction progress at a high iron:protein ratio was followed after the addition of 20 Fe^{2+} ions per subunit as the change of $A_{350\ nm}$ using rapid mixing (less than 10 ms) of 50 μM protein subunits (2.08 μM protein cages) in 200 mM MOPS, 200 mM NaCl, pH 7.0, with an equal volume of freshly prepared 1 mM ferrous sulfate in 1 mM HCl; the same UV-visible stopped-flow spectrophotometer was used, and 4000 data points were routinely collected in 1000 s (44, 45). Rates of DFO(H) miner-

alization were calculated from the linear fitting of the initial phases of the 350-nm traces.

Author Contributions—B. C. performed all MD simulations and analyzed the results. C. B. performed the iron uptake kinetic experiments on all ferritin variants. D. D. M. analyzed the atomistic simulation results together with B. C. B. C., P. T., and G. B. conceived the idea for the project and wrote the paper. All authors reviewed the results and approved the final version of the manuscript.

Acknowledgments—We kindly acknowledge the SMART@SNS Laboratory technical staff for managing the computing facilities at the Scuola Normale Superiore (SNS). We kindly acknowledge Prof. Stefano Mangani for providing the X-ray crystal structures and for useful discussions.

References

1. Arosio, P., Carmona, F., Gozzelino, R., Maccarinelli, F., and Poli, M. (2015) The importance of eukaryotic ferritins in iron handling and cytoprotection. *Biochem. J.* **472,** 1–15
2. Theil, E. C., Tosha, T., and Behera, R. K. (2016) Solving biology's iron chemistry problem with ferritin protein nanocages. *Acc. Chem. Res.* **49,** 784–791
3. Bou-Abdallah, F. (2010) The iron redox and hydrolysis chemistry of the ferritins. *Biochim. Biophys. Acta* **1800,** 719–731
4. Honarmand Ebrahimi, K., Hagedoorn, P.-L., and Hagen, W. R. (2015) Unity in the biochemistry of the iron-storage proteins ferritin and bacterioferritin. *Chem. Rev.* **115,** 295–326
5. Takahashi, T., and Kuyucak, S. (2003) Functional properties of threefold and fourfold channels in ferritin deduced from electrostatic calculations. *Biophys. J.* **84,** 2256–2263
6. Chasteen, N. D. (1998) Ferritin: uptake, storage, and release of iron. *Met. Ions Biol. Syst.* **35,** 479–514
7. Harrison, P. M., and Arosio, P. (1996) The ferritins: molecular properties, iron storage function and cellular regulation. *Biochim. Biophys. Acta* **1275,** 161–203
8. Bernacchioni, C., Ghini, V., Theil, E. C., and Turano, P. (2016) Modulating the permeability of ferritin channels. *RSC Adv.* **6,** 21219–21227
9. Behera, R. K., Torres, R., Tosha, T., Bradley, J. M., Goulding, C. W., and Theil, E. C. (2015) Fe^{2+} substrate transport through ferritin protein cage ion channels influences enzyme activity and biomineralization. *J. Biol. Inorg. Chem.* **20,** 957–969
10. Theil, E. C., Takagi, H., Small, G. W., He, L., Tipton, A. R., and Danger, D. (2000) The ferritin iron entry and exit problem. *Inorg. Chim. Acta* **297,** 242–251
11. Levi, S., Santambrogio, P., Corsi, B., Cozzi, A., and Arosio, P. (1996) Evidence that residues exposed on the three-fold channels have active roles in the mechanism of ferritin iron incorporation. *Biochem. J.* **317,** 467–473
12. Pozzi, C., Di Pisa, F., Lalli, D., Rosa, C., Theil, E., Turano, P., and Mangani, S. (2015) Time-lapse anomalous X-ray diffraction shows how Fe^{2+} substrate ions move through ferritin protein nanocages to oxidoreductase sites. *Acta Crystallogr. D* **71,** 941–953
13. Pozzi, C., Di Pisa, F., Bernacchioni, C., Ciambellotti, S., Turano, P., and Mangani, S. (2015) Iron binding to human heavy-chain ferritin. *Acta Crystallogr. D* **71,** 1909–1920
14. Jutz, G., van Rijn, P., Santos Miranda, B., and Böker, A. (2015) Ferritin: a versatile building block for bionanotechnology. *Chem. Rev.* **115,** 1653–1701
15. Heger, Z., Skalickova, S., Zitka, O., Adam, V., and Kizek, R. (2014) Apoferritin applications in nanomedicine. *Nanomedicine* **9,** 2233–2245
16. Vasalatiy, O., Zhao, P., Zhang, S., Aime, S., and Sherry, A. D. (2006) Catalytic effects of apoferritin interior surface residues on water proton exchange in lanthanide complexes. *Contrast Media Mol. Imaging* **1,** 10–14
17. Aime, S., Frullano, L., and Geninatti Crich, S. (2002) Compartmentalization of a gadolinium complex in the apoferritin cavity: a route to obtain high relaxivity contrast agents for magnetic resonance imaging. *Angew. Chem. Int. Ed. Engl.* **41,** 1017–1019
18. Liu, X., and Theil, E. C. (2005) Ferritins: dynamic management of biological iron and oxygen chemistry. *Acc. Chem. Res.* **38,** 167–175
19. Haldar, S., Bevers, L. E., Tosha, T., and Theil, E. C. (2011) Moving iron through ferritin protein nanocages depends on residues throughout each four α-helix bundle subunit. *J. Biol. Chem.* **286,** 25620–25627
20. Bernacchioni, C., Pozzi, C., Di Pisa, F., Mangani, S., and Turano, P. (2016) Ferroxidase activity in eukaryotic ferritin is controlled by accessory-iron-binding sites in the catalytic cavity. *Chemistry* **22,** 16213–16219
21. Hwang, J., Krebs, C., Huynh, B. H., Edmondson, D. E., Theil, E. C., and Penner-Hahn, J. E. (2000) A short Fe-Fe distance in peroxodiferric ferritin: control of Fe substrate versus cofactor decay? *Science* **287,** 122–125
22. Bertini, I., Lalli, D., Mangani, S., Pozzi, C., Rosa, C., Theil, E. C., and Turano, P. (2012) Structural insights into the ferroxidase site of ferritins from higher eukaryotes. *J. Am. Chem. Soc.* **134,** 6169–6176
23. Behera, R. K., and Theil, E. C. (2014) Moving Fe^{2+} from ferritin ion channels to catalytic OH centers depends on conserved protein cage carboxylates. *Proc. Natl. Acad. Sci. U.S.A.* **111,** 7925–7930
24. Beckstein, O., and Sansom, M. S. (2004) The influence of geometry, surface character, and flexibility on the permeation of ions and water through biological pores. *Phys Biol.* **1,** 42–52
25. Chandramouli, B., Di Maio, D., Mancini, G., Barone, V., and Brancato, G. (2015) Breaking the hydrophobicity of the MscL pore: insights into a charge-induced gating mechanism. *PLoS One* **10,** e0120196
26. Aryal, P., Sansom, M. S. P., and Tucker, S. J. (2015) Hydrophobic gating in ion channels. *J. Mol. Biol.* **427,** 121–130
27. Di Maio, D., Chandramouli, B., and Brancato, G. (2015) Pathways and barriers for ion translocation through the 5-HT_3A receptor channel. *PLoS One* **10,** e0140258
28. Åqvist, J., and and Luzhkov, V. (2000) Ion permeation mechanism of the potassium channel. *Nature* **404,** 881–884
29. Laghaei, R., Evans, D. G., and Coalson, R. D. (2013) Metal binding sites of human H-chain ferritin and iron transport mechanism to the ferroxidase sites: A molecular dynamics simulation study. *Proteins* **81,** 1042–1050
30. Banghart, M. R., Volgraf, M., and Trauner, D. (2006) Engineering light-gated ion channels. *Biochemistry* **45,** 15129–15141
31. Chandramouli, B., Di Maio, D., Mancini, G., and Brancato, G. (2016) Introducing an artificial photo-switch into a biological pore: a model study of an engineered α-hemolysin. *Biochim. Biophys. Acta* **1858,** 689–697
32. Hornak, V., Abel, R., Okur, A., Strockbine, B., Roitberg, A., and Simmerling, C. (2006) Comparison of multiple Amber force fields and development of improved protein backbone parameters. *Proteins* **65,** 712–725
33. Li, P., Roberts, B. P., Chakravorty, D. K., and Merz, K. M. (2013) Rational design of particle mesh Ewald compatible Lennard-Jones parameters for +2 metal cations in explicit solvent. *J. Chem. Theory Comput.* **9,** 2733–2748
34. Ryckaert, J.-P., Ciccotti, G., and Berendsen, H. J. C. (1977) Numerical integration of the cartesian equations of motion of a system with constraints: molecular dynamics of *n*-alkanes. *J. Comput. Phys.* **23,** 327–341
35. Darden, T., York, D., and Pedersen, L. (1993) Particle mesh Ewald: an $N\cdot\log(N)$ method for Ewald sums in large systems. *J. Chem. Phys.* **98,** 10089–10089
36. Izaguirre J. s., A., Catarello, D. P., Wozniak, J. M., and and Skeel, R. D. (2001) Langevin stabilization of molecular dynamics. *J. Chem. Phys.* **114,** 2090–2090
37. Smart, O. S., Neduvelil, J. G., Wang, X., Wallace, B. A., and Sansom, M. S. (1996) HOLE: a program for the analysis of the pore dimensions of ion channel structural models. *J. Mol. Graph.* **14,** 354–360, 376
38. Michaud-Agrawal, N., Denning, E. J., Woolf, T. B., and Beckstein, O. (2011) MDAnalysis: a toolkit for the analysis of molecular dynamics simulations. *J. Comput. Chem.* **32,** 2319–2327

39. Pettersen, E. F., Goddard, T. D., Huang, C. C., Couch, G. S., Greenblatt, D. M., Meng, E. C., and Ferrin, T. E. (2004) UCSF Chimera: a visualization system for exploratory research and analysis. *J. Comput. Chem.* **25,** 1605–1612
40. Hunter, J. D. (2007) Matplotlib: a 2D graphics environment. *Comput. Sci. Eng.* **9,** 90–95
41. Darve, E., and Pohorille, A. (2001) Calculating free energies using average force. *J. Chem. Phys.* **115,** 9169–9169
42. Darve, E., Rodríguez-Gómez, D., and Pohorille, A. (2008) Adaptive biasing force method for scalar and vector free energy calculations. *J. Chem. Phys.* **128,** 144120–144120
43. Bernacchioni, C., Ghini, V., Pozzi, C., Di Pisa, F., Theil, E. C., and Turano, P. (2014) Loop electrostatics modulates the intersubunit interactions in ferritin. *ACS Chem. Biol.* **9,** 2517–2525
44. Theil, E. C., Turano, P., Ghini, V., Allegrozzi, M., and Bernacchioni, C. (2014) Coordinating subdomains of ferritin protein cages with catalysis and biomineralization viewed from the C. *J. Biol. Inorg. Chem.* **19,** 615–622
45. Bernacchioni, C., Ciambellotti, S., Theil, E. C., and Turano, P. (2015) Is His54 a gating residue for the ferritin ferroxidase site? *Biochim. Biophys. Acta* **1854,** 1118–1122

Electrostatic and Structural Bases of Fe^{2+} Translocation Through Ferritin Channels

Balasubramanian Chandramouli, Caterina Bernacchioni, Danilo Di Maio, Paola Turano and Giuseppe Brancato

Supporting Information

Content

Table S1: Summary of simulated ferritin channel models

Model	Description	Time (ns)
C3WT*	Wild type C3 channel	100
C3SM*	Single mutant C3 (E130A)	100
C3TM	Triple mutant C3 (D127A,E130A,S131A)	100
C4WT	Wild type C4 channel	100
C4TM	Triple mutant C4 (M161D,L165D,H169D)	100

*Simulated both in the presence and absence of Fe^{2+} ions in the channel

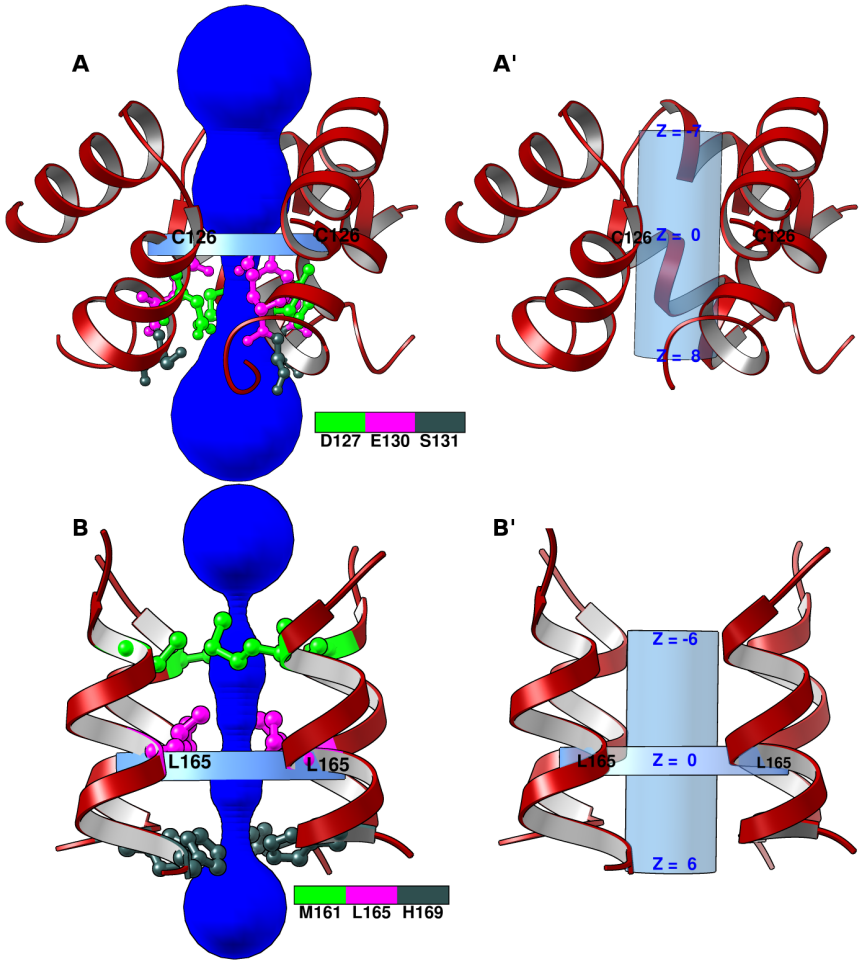

Figure S1. C3 and C4 ferritin channels. Pictorial representations of the channel radius estimation and transition coordinate for PMF profile. The reference point (i.e., Z=0) in C3 systems was set to the C_α centroid of C126 and in C4 systems was set to the C_α centroid of L165.

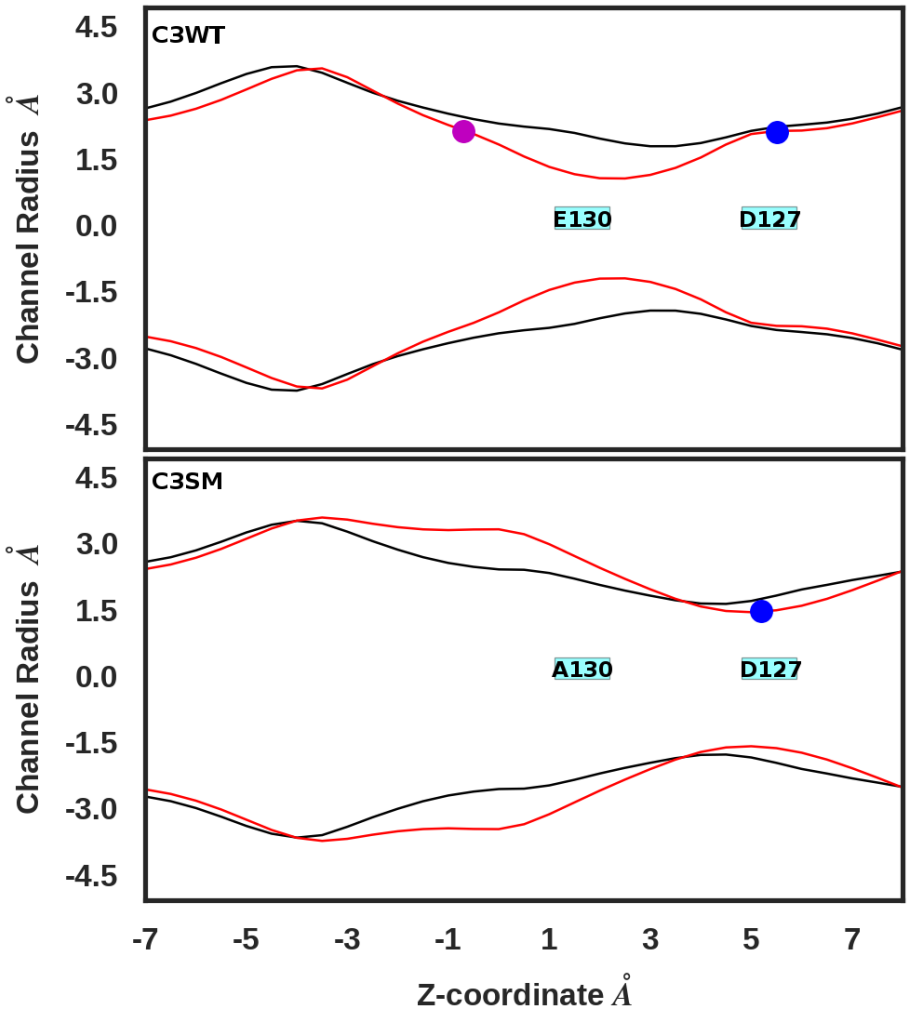

Figure S2. C3 channel radius analysis. Ferritin channel radius as a function of Z-coordinate issuing from the C3WT and C3SM simulations, in presence (red) and absence (black) of Fe^{2+} ions. Filled circles show the average positions of Fe^{2+} ions during the MD simulation.

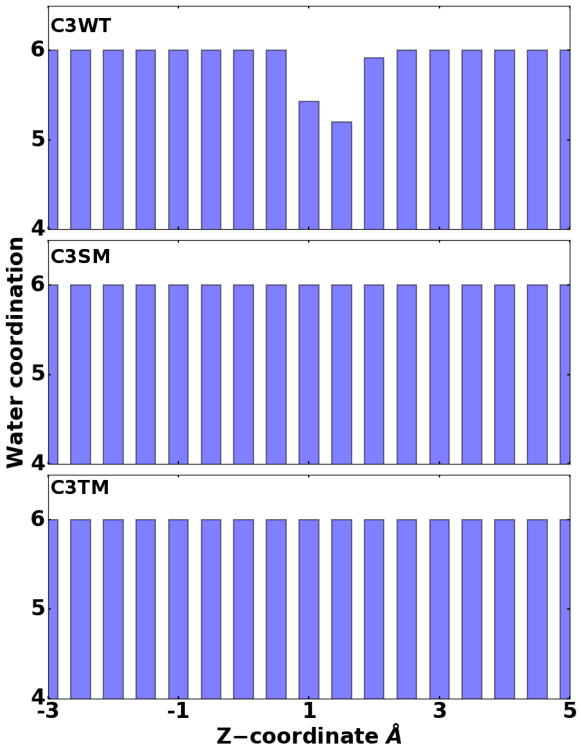

Figure S3. Water coordination around Fe^{2+}. Water coordination number in the first hydration layer of Fe^{2+} as a function of Z-coordinate, as issuing from C3WT, C3SM and C3TM PMF simulations.

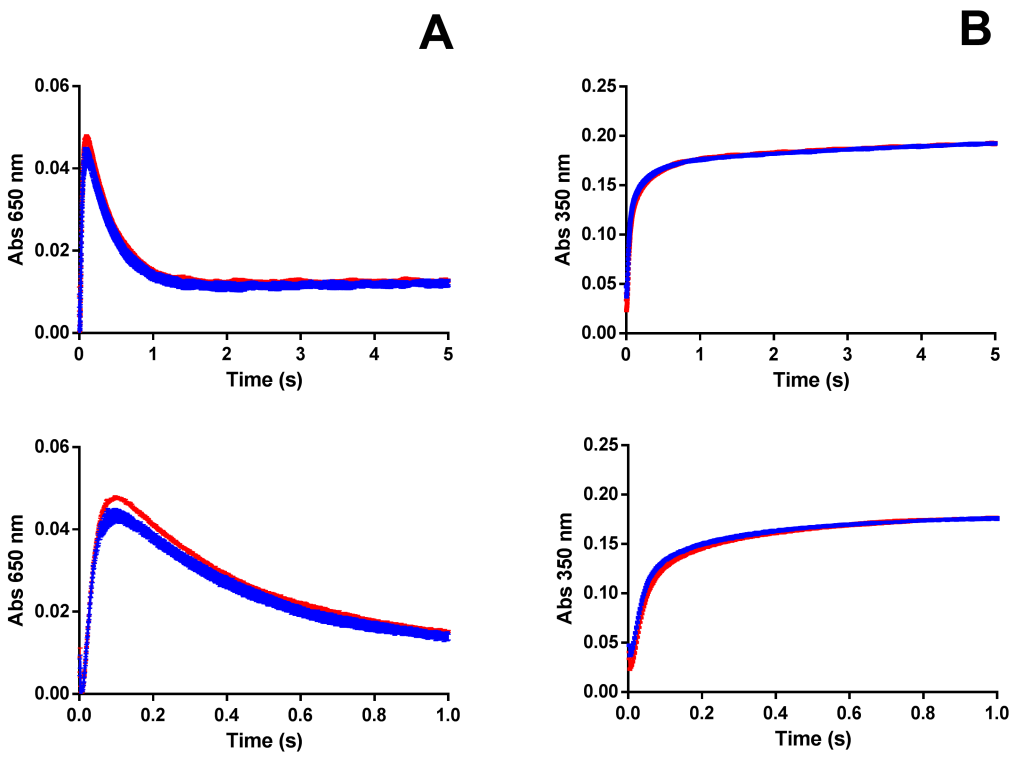

Figure S4. Wild-type vs C126A iron-uptake rate, single turnover reaction. Kinetics of products formation in wild-type (blue) and C126A (red) ferritin by rapid-mixing, UV–vis spectroscopy following the addition of 2 Fe^{2+}/subunit. Formation of (A) DFP intermediate ($A_{650\ nm}$) and (B) DFO(H) products ($A_{350\ nm}$); the lower panels show enlargements of the first second to highlight the likeness in the initial rates. Each graph shows a set of curves (mean±SD) of a representative experiment of three.

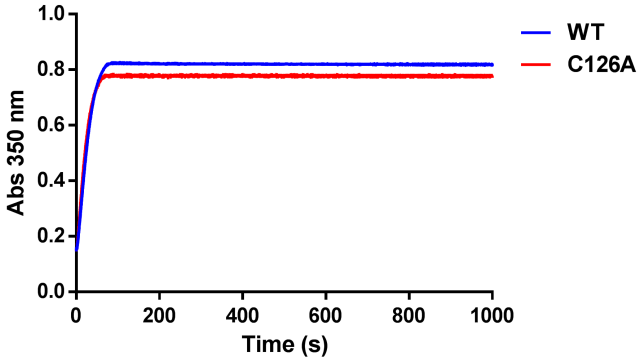

Figure S5. Wild-type vs C126A reaction progress at high iron:protein ratio. Kinetics of products formation in wild-type (blue) and C126A (red) ferritin by rapid-mixing, UV–vis spectroscopy at high iron:protein ratio (20 Fe^{2+}/subunit; 480 Fe^{2+}/cage) monitored as DFO(H) products ($A_{350\ nm}$) formation.

Electrostatic and Structural Bases of Fe^{2+} Translocation through Ferritin Channels

Balasubramanian Chandramouli, Caterina Bernacchioni, Danilo Di Maio, Paola Turano and Giuseppe Brancato

J. Biol. Chem. 2016, 291:25617-25628.
doi: 10.1074/jbc.M116.748046 originally published online October 18, 2016